

# Geochemistry, Geophysics, Geosystems

## RESEARCH ARTICLE

10.1029/2018GC007478

### Key Points:

- The seasonal variations of the hum are larger in the northern hemisphere than the southern hemisphere
- The data-model fit confirms the interaction between infragravity waves and the continental slope as the main source of the hum
- The hum is sensitive to local sources generated by the passage of a cyclone

### Supporting Information:

- Supporting Information S1
- Movie S1

### Correspondence to:

E. Stutzmann,  
stutz@ipggp.fr

### Citation:

Deen, M., Stutzmann, E., & Arduin, F. (2018). The Earth's hum variations from a global model and seismic recordings around the Indian Ocean. *Geochemistry, Geophysics, Geosystems*, 19, 4006–4020. <https://doi.org/10.1029/2018GC007478>

Received 6 FEB 2018

Accepted 2 SEP 2018

Accepted article online 11 SEP 2018

Published online 27 OCT 2018

## The Earth's Hum Variations From a Global Model and Seismic Recordings Around the Indian Ocean

M. Deen<sup>1</sup> , E. Stutzmann<sup>1</sup> , and F. Arduin<sup>2</sup>

<sup>1</sup>Institut de Physique du Globe, de Paris, CNRS-UMR7154, Paris, France, <sup>2</sup>University of Brest, CNRS, IFREMER, IRD, LOPS, Plouzané, France

**Abstract** The Earth's hum is the continuous oscillations of the Earth at frequencies between 2 and 20 mHz in the absence of earthquakes. The hum strongest signal consists mainly of surface waves. These seismic waves can be generated by infragravity waves propagating over a sloping ocean bottom close to the coast. So far, this theory has only been tested quantitatively using European seismic stations. We use seismic data recorded all around the Indian Ocean together with an ocean wave model that provides time-frequency varying hum sources. We show that seasonal variations of the hum sources are smaller in the southern hemisphere than the northern hemisphere. Using these sources, we model Rayleigh wave root-mean-square amplitudes in the frequency band 3.5–20 mHz, and the good agreement with seismic data on the vertical component confirms the theory of hum generation. Because the Indian Ocean is uniquely connected to the southern hemisphere oceans but lies partly in northern hemisphere latitudes, the seasonal pattern of the hum recorded there is particular and shows no significant seasonal variations. At ~10 mHz the hum is strongly influenced by local events, such as the passage of a cyclone close to a seismic station.

**Plain Language Summary** In the absence of earthquake, the solid Earth is continuously vibrating at very low frequencies (2 to 20 mHz). These vibrations, called seismic hum, were discovered in the 1990s and can be recorded by seismic stations everywhere on Earth. These vibrations have frequencies least a thousand times lower than audible sound, and should not be confused with the persistent sounds - that are also called hum - that can be heard in different regions. They are generated by ocean infragravity waves propagating over a sloping ocean bottom close to the coast. So far, this theory has only been tested quantitatively using European seismic stations. We analyze seismic data recorded all around the Indian Ocean, and we model them using hum sources derived from an ocean wave model. The good fit between data and model confirms the theory of hum generation. We further show that the hum recorded in the Indian Ocean is very specific and displays no significant seasonal variations. Finally, we demonstrate that when a cyclone arrives at a coast, it creates hum sources that increase the very low frequency seismic signal recorded by the nearby stations.

## 1. Introduction

In the absence of earthquakes, seismic stations record the Earth's continuous oscillations, known as the hum, in the frequency band 2 and 20 mHz. The hum can be used for ambient noise tomography. Nishida et al. (2009) obtained a tomographic model of the upper mantle, by using the hum recorded during 15 years at periods between 120 and 375 s. Haned et al. (2015) extracted the empirical Green's function from the hum signal in the period band 30–250 s and obtained a global tomographic model of the Earth's upper mantle using only 2 years of data. These models are derived from surface wave dispersion measurements. In order to perform full waveform inversion of the empirical Green's functions, a better understanding of the spatial and temporal distribution of the hum sources is needed (e.g., Fichtner, 2014; Tromp et al., 2010).

The hum was first observed on gravimeters by Nawa et al. (1998) and Suda et al. (1998) and on vertical STS1 seismometers by Kobayashi and Nishida (1998) and Tanimoto et al. (1998). Since then, seismic hum has been observed on more than 200 land stations (Nishida, 2013). Recently, Deen et al. (2017) observed the hum signal for the first time on two ocean-bottom seismometers in the Indian Ocean. The hum amplitude differs between summer and winter months (Ekström, 2001; Kurrle & Widmer-Schmidrig, 2006; Nishida & Fukao, 2007; Roult & Crawford, 2000; Tanimoto & Um, 1999), though this seasonal difference is not observed everywhere (Deen et al., 2017; Rhie & Romanowicz, 2006; Tanimoto & Um, 1999).

Many small earthquakes are not enough to explain the measured hum amplitudes and seasonality (Ekström, 2001; Kobayashi & Nishida, 1998; Suda et al., 1998; Tanimoto & Um, 1999), and several theories have been

proposed to explain the observed signals. Below 2 mHz, the signal is dominated by gravitational effects (Widmer-Schmidrig, 2003). Above 2 mHz, random pressure disturbances over the Earth surface were considered to approximate the hum spheroidal mode amplitudes (Fukao et al., 2002; Kobayashi & Nishida, 1998; Nishida & Kobayashi, 1999; Tanimoto & Um, 1999). However, atmospheric excitation mechanisms cannot explain the broad noise peak observed above 5 mHz (e.g., Nishida, 2013; Tanimoto, 2005).

Seismic data are consistent with hum sources distributed globally along the coasts (Bromirski & Gerstoft, 2009; Rhie & Romanowicz, 2004, 2006; Webb, 2008) or in shallow water (Tanimoto, 2005), and many theories have linked the hum with ocean waves. These include the effects of ocean infragravity waves, acting on the seafloor via horizontal forces resulting from the pressure acting on a sloping bottom (Nishida et al., 2008), or vertical forces, possibly involving the interaction of different surface gravity wave trains, as reviewed by Nishida (2013). Ocean infragravity waves are long-period (30–300 s), low-amplitude (<10 cm), long-wavelength (1–40 km) surface ocean gravity waves that are generated at the shoreline, from wind sea and swell wave components (Bertin et al., 2018; Hasselmann, 1962; Longuet-Higgins & Stewart, 1962).

Theories relying on interacting ocean waves of frequency  $f$  and  $f'$  giving a seismic wave of frequency  $f + f'$  (Webb, 2007, 2008) generally missed the pressure induced by ocean waves on the bottom, which cancels the surface pressure in the limit of longwave periods (Ardhuin & Herbers, 2013). The other interaction giving  $f - f'$  was considered by Traer and Gerstoft (2014) but does not excite significant seismic waves in horizontally homogeneous conditions, because the interaction produces patterns that travel slower than the group speed of ocean waves, typically less than 30 m/s. The only theory that was verified in terms of temporal variations of seismic spectra is the effect of pressure sources generated by infragravity waves propagating over a sloping bottom proposed by Ardhuin et al. (2015). This mechanism was first outlined by Hasselmann (1963) for explaining the primary microseisms at periods around 15 s. This mechanism can explain Rayleigh waves, but it cannot explain Love waves observed in the hum period band on horizontal component (Kurrle & Widmer-Schmidrig, 2008; Nishida et al., 2008).

In Ardhuin et al. (2015), four seismic stations, all located in Europe, were used to verify that the theory could predict the amplitude and temporal variations of the hum. Here we carry out a more extended study using a larger data set, with the objective of understanding the spatial and temporal variation of hum sources. We use the approach of Ardhuin et al. (2015) that is the numerical modeling of infragravity waves to obtain the pressure sources along the coasts, which we use to model Rayleigh wave root-mean-square (RMS) amplitude recorded by seismic stations in and around the Indian Ocean. The Indian Ocean is located partly at northern and partly at southern latitudes and is opened to oceans in the southern hemisphere (SH), making it particularly suitable to study temporal and spatial variability of the hum in the SH.

## 2. Computing the Hum Sources From Ocean Waves

We use the pressure model in the hum frequency band of Ardhuin et al. (2015) resulting from the interaction of infragravity waves with continental shelves. The numerical wave code WAVEWATCH III version 5.01 (Tolman et al., 2014) is used in a global configuration and calculates ocean wave directional spectra in grids with a resolution of  $0.5^\circ$  in latitude and longitude, every 3 hr. The wave spectrum is discretized in 36 directions, and 58 frequencies exponentially spaced from 3.1 to 720 mHz. This extension to low frequencies compared to usual wave models is described in Ardhuin et al. (2014). It consists of sources of infragravity waves parameterized from the total energy and mean period of the lower frequency components. Except for the spectral resolution, all other model parameters are identical to the model configuration validated in detail by Rasche and Ardhuin (2013). The model is forced every 3 hr by wind data from the European Center for Medium range Weather Forecasting (ECMWF). The model also uses sea ice concentration from the Climate Forecast System Reanalysis (Saha et al., 2010), and iceberg concentrations derived from satellite altimeter data (Ardhuin et al., 2011; Tournadre et al., 2016).

In this section, waves are ocean infragravity waves unless specified otherwise. Following Hasselmann (1963) and Ardhuin et al. (2015), we consider that the water depth is uniform along the shore. In that case, the generation of seismic waves at the same frequency as the ocean waves involves waves propagating toward the shore in direction  $\theta_n$  and in the opposite direction ( $\theta_n + \pi$ ). Because the wave properties evolve in the cross-shore direction, we use for reference the wave frequency-direction spectrum at a given location  $A$  outside of the surf zone. For any frequency  $f$ , the power spectral densities  $E_A(f, \theta_n)$  and  $E_A(f, \theta_n + \pi)$  are transformed by

refraction (Longuet-Higgins, 1957; O'Reilly & Guza, 1993) and characterize the energy of waves traveling toward and away from the coast and their spectral densities. The latter waves are generally more energetic because their source is at the nearest shoreline, at a very short distance (e.g., Neale et al., 2015; Rawat et al., 2014). In practice, we specify pressure power spectral density (PSD) at points adjacent to land and treat separately the islands that are resolved by the grid and those that are smaller than the grid. For the resolved land, the determination of shore-normal direction is explained in Arduin and Roland (2012) and uses the shape of the land-sea mask. For unresolved islands, a pressure PSD proportional to the along-shore distance  $L_y$  is decomposed in 36 sources around the grid cell where islands are present, every  $10^\circ$  in azimuth.

Although the frequency of ocean waves is conserved, the wavenumber  $k_A$  of ocean waves changes along the bathymetry profile so that the dispersion relationship for linear waves is fulfilled. At location  $A$  with ocean depth  $D_A$ , it is,  $(2\pi f)^2 = gk_A \tanh(k_A D_A)$ , where  $g$  is the gravitational acceleration.

The seafloor pressure PSD,  $F_p(f)$ , at depth  $D_A$ , is

$$F_p(f) = s \frac{\rho_w^2 g^4}{k_A^2 32 L_x} [E_A(f, \theta_n) + E_A(f, \theta_n + \pi)] \quad (1)$$

where  $s/32$  is a dimensionless parameter that is function of the bottom topography and the wave frequency  $f$  (see Eq. 4.27 of Hasselmann, 1963),  $\rho_w$  is the water density, and  $L_x$  is the cross-shore distance over which the pressure PSD is calculated. This spectral density corresponds to the effect of waves on the entire depth profile extending to infinity. In practice, similar values are obtained for realistic profiles. Further, the portion of the depth profile that appears to contribute most to the pressure spectrum is around the intermediate depth  $D$  such that the ocean wavenumber at that depth  $k$  satisfies  $kD = 0.76$  (Arduin et al., 2015). For a frequency of 10 mHz this depth is 1,200 m.

The PSD  $F_p(f)$  is a power density in wavenumber ( $k_x, k_y$ ) and frequency space, with units of  $\text{Pa}^2 \text{m}^2 \text{s}$ . In practice, it varies very slowly with the horizontal seismic wavenumber vector ( $k_x, k_y$ ).

Therefore, the sea-bottom pressure spectrum is broad enough to generate all seismic phases that can be excited by vertical forces on a flat surface, with an isotropic radiation pattern. We can use the expression given by Longuet-Higgins (1950) for computing the seismic source term due to pressure PSD applied on any surface of dimension  $L_x L_y$  (typically  $50 \times 50 \text{ km}^2$  in our model). In the particular case of shallow water depth with respect to frequency:

$$S(f) = \frac{4\pi^2 f c^2}{\beta^5 \rho^2} F_p(f) L_x L_y \quad (2)$$

where  $\beta$  and  $\rho$  are the  $S$  wave velocity and density in the crust and  $c$  is a nondimensional coefficient that corresponds to the Rayleigh wave source site effect in a two-layer ocean-crust medium (Arduin & Herbers, 2013; Longuet-Higgins, 1950). The water depth  $D_A$  (1,200 m) is small compared to seismic wavelength (about 300 km for a frequency  $f = 0.01$  Hz), and therefore, we use  $c\left(\frac{2\pi f D}{\beta} = 0\right)$  given by Longuet-Higgins (1950). Gualtieri et al. (2013) showed that this coefficient  $c$  can be computed, for any Earth model, as the normalized product of the vertical eigen-function amplitudes taken at the source and receiver depths divided by the angular frequency. Their Figure 2 shows that there is no difference between  $c(0)$  for a two-layer (ocean-crust) model or PREM.

We can now compute the PSD of the vertical seismic acceleration by summing up the contribution of each source  $S_i(f)$  at angular distance  $\Delta_i$ , taking into account seismic attenuation and geometrical spreading for the R1 and R2 Rayleigh wave trains and multiple orbits around the Earth:

$$F_\delta(f) = \sum_i (2\pi f)^4 \frac{S_i(f)}{R_E} \left[ \frac{\exp\left(\frac{-2\pi f \Delta_i R}{Q(f)U(f)}\right)}{\sin \Delta_i} + \frac{\exp\left(\frac{-2\pi f (2\pi - \Delta_i) R}{Q(f)U(f)}\right)}{\sin(2\pi - \Delta_i)} \right] \frac{1}{1-b} \quad (3)$$

where  $R$  is the Earth radius,  $Q(f)$  is the seismic attenuation, and  $U(f)$  is the group velocity for the Rayleigh wave fundamental mode. Attenuation and group velocities are computed for model QL6 (Durek & Ekstrom, 1996) and PREM (Dziewonski & Anderson, 1981), respectively. The surface wave attenuation over one orbit around

the Earth is given by  $b = \exp\left(\frac{-(2\pi)^2 f R_E}{Q(f)U(f)}\right)$ , and  $\frac{1}{1-b} = 1 + b + b^2 + b^3 \dots$  represents the incoherent sum of the energies of all the orbits.

### 3. Temporal and Spatial Variations of Hum Sources

In this section, we investigate the hum sources at global scale. The seasonal pattern of the modeled pressure PSD along coasts (equation (1)) averaged in the frequency band 7–20 mHz is shown in Figure 1 and follows that of the infragravity wave heights (Ardhuin et al., 2014; Aucan & Ardhuin, 2013).

In the SH, pressure PSD stronger than 85 dB with respect to  $\text{Pa}^2/(\text{m}^{-2} \text{Hz})$  is present year round. The northern part of the Indian Ocean, although in the northern hemisphere (NH), follows the same seasonal variation as the SH, with weaker sources and a weaker annual variations compared to the southern part of the Indian Ocean.

The NH pressure PSD shows seasonal variations, with higher PSD during NH winter (January–February–March). Table 1 gives the maximum values of the average pressure PSD for SH summer (January, February, and March) and SH winter (July, August, and September). We find that the ratio of the maximum PSD of pressure in winter/summer is larger for the NH (3.4) than for the SH (1.8). We also see that during NH summer (July, August, and September) the maximum pressure PSD in the SH is in the same order of magnitude as in the NH. The difference between NH summer and winter is marked in blue in Figure 1c, and the largest absolute difference is localized at the west coast of North America, Europa, and West Africa down to the equator and at the east coast of Greenland.

Figure 1 also shows that in general the strongest sources are located on the west coasts of the continents, together with the east coast of southern Africa and Madagascar, and of Greenland and Siberia. Stutzmann et al. (2012) found a similar pattern for secondary microseism coastal sources. We note that interactions between ocean wave and sea ice are not yet fully quantified in the model, leaving sources around Antarctica out of the interpretation.

### 4. Data Selection and Computing the Seismic Spectra

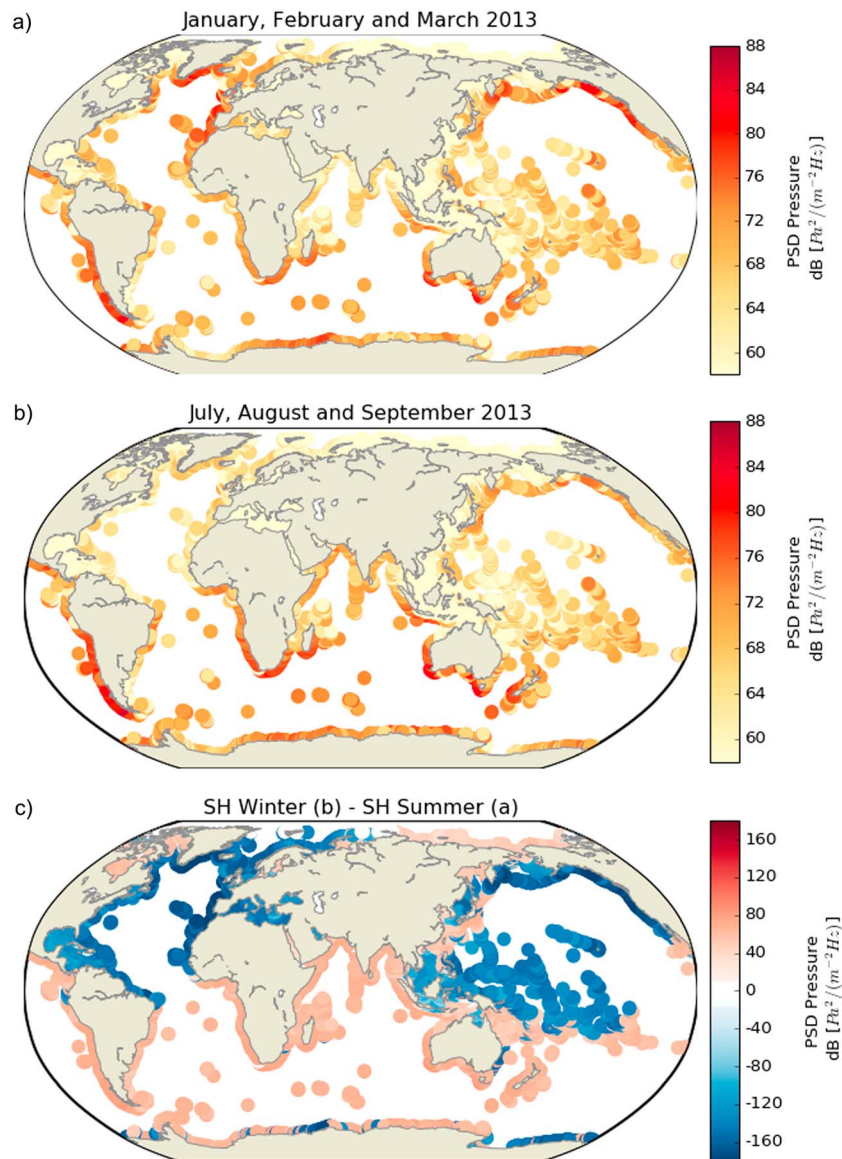
We selected data based on a threshold of minimum 90% data availability for the year 2013 for stations within  $50^\circ$  radius around the Indian Ocean (latitude =  $-23.64$ , longitude =  $75.50$ ). We removed the instrument response. Afterward, we performed a quality control check using probabilistic power spectral densities where stations with a signal level above  $-175$  dB with respect to acceleration (for frequencies between 2 and 20 mHz), for more than 20% of the time, were eliminated and we ended up with 17 stations. Finally, we visually chose seven stations based on their lowest noise levels to present in this paper and supporting information. This operation removed all ocean bottom from the RHUM-RUM experiment (Barruol & Sigloch, 2013) that in general have a high noise level in the hum period band (Duennebieer & Sutton, 1995) as well island stations. We computed spectra on prolate tapered windows of length 2048 s, considering 50% data overlap, and we computed the PSD over each 3-hr windows (e.g., Stutzmann et al., 2000).

Figure 2 shows the location of the stations and the yearly averaged PSD with respect to acceleration for the data (blue) and the model (red) for the year 2013. The station names in bold (LBTB, VOI, JAGI, and WRKA) are discussed hereafter. The other stations (LSZ, ABPO, and PLAI) are discussed in the supporting information.

For computing the fit between the annual median of the observed and synthetic PSD, we remove recordings of earthquakes of magnitude  $M_w$  larger than 5.6 following the criterion used in Ekström (2001):

$$T = 2.5 + 40(M_w - 5.6)$$

where  $T$  is the duration of data removed in hours after the earthquake. We use these data to determine empirically the  $s$  value (see equation (1)) as follows. We use data and synthetics for time sequences without earthquake and averaged in the frequency range 10–15 mHz. For each station, we select the  $s$  value that provides the best fit between the model and data PSD. Later, using these same values of  $s$ , we use continuous data (without earthquake removal) to study the seismic hum seasonality and the relation to source location. Figure 2 shows that we obtain a good agreement between modeled and observed seismic hum PSD for  $s$  values between 3 and 4%.



**Figure 1.** Seismic hum sources. Modeled pressure power spectral density (PSD) averaged in the frequency band 7–20 mHz over (a) January-February-March and (b) July-August-September 2013. In (a), northern hemisphere (NH) winter is shown with strong sources along the west coasts; sources in the northern part of the Indian Ocean have low amplitudes. Strong sources appear on the west coasts of Europe, northern America, and Africa, as well as the east coast of Greenland. In (b), southern hemisphere (SH) winter is shown, with strong sources around the west coasts of South America, Africa, Australia, New Zealand, and Indonesia. Other strong sources are along Antarctica coasts. Pressure PSD increases around the west coast of India, the east of the Arabic peninsula, and Madagascar, as well as the east of southern Africa. In (c) we subtracted (a) from (b), and we see positive values in the SH. We observe positive values in the entire Indian Ocean, whereas in the western Pacific Ocean values are negative at similar latitudes close and above the equator.

**Table 1**

Maximum Pressure PSD in  $\text{Pa}^2/(\text{m}^{-2} \text{Hz})$  in the SH and the NH Averaged Over 3 Months Corresponding to SH Summer (January, February, and March 2013) and SH Winter (July, August, and September 2013)

Max PSD pressure	SH	NH
SH summer (January-February-March)	$2.17 * 10^8$	$2.24 * 10^8$
SH winter (June-July-August)	$3.92 * 10^8$	$6.57 * 10^7$

## 5. Temporal Variations of the Seismic Hum Recorded in the Indian Ocean

We first investigate temporal variations of the observed and modeled hum RMS averaged between 7 and 20 mHz over the year 2013 at the four stations LBTB, VOI, JAGI, and WRKA.

Figure 3 shows the comparison between data (blue) and the synthetic (red) RMS amplitudes during the different seasons. Results for the other stations are in the supporting information. In the following explanations

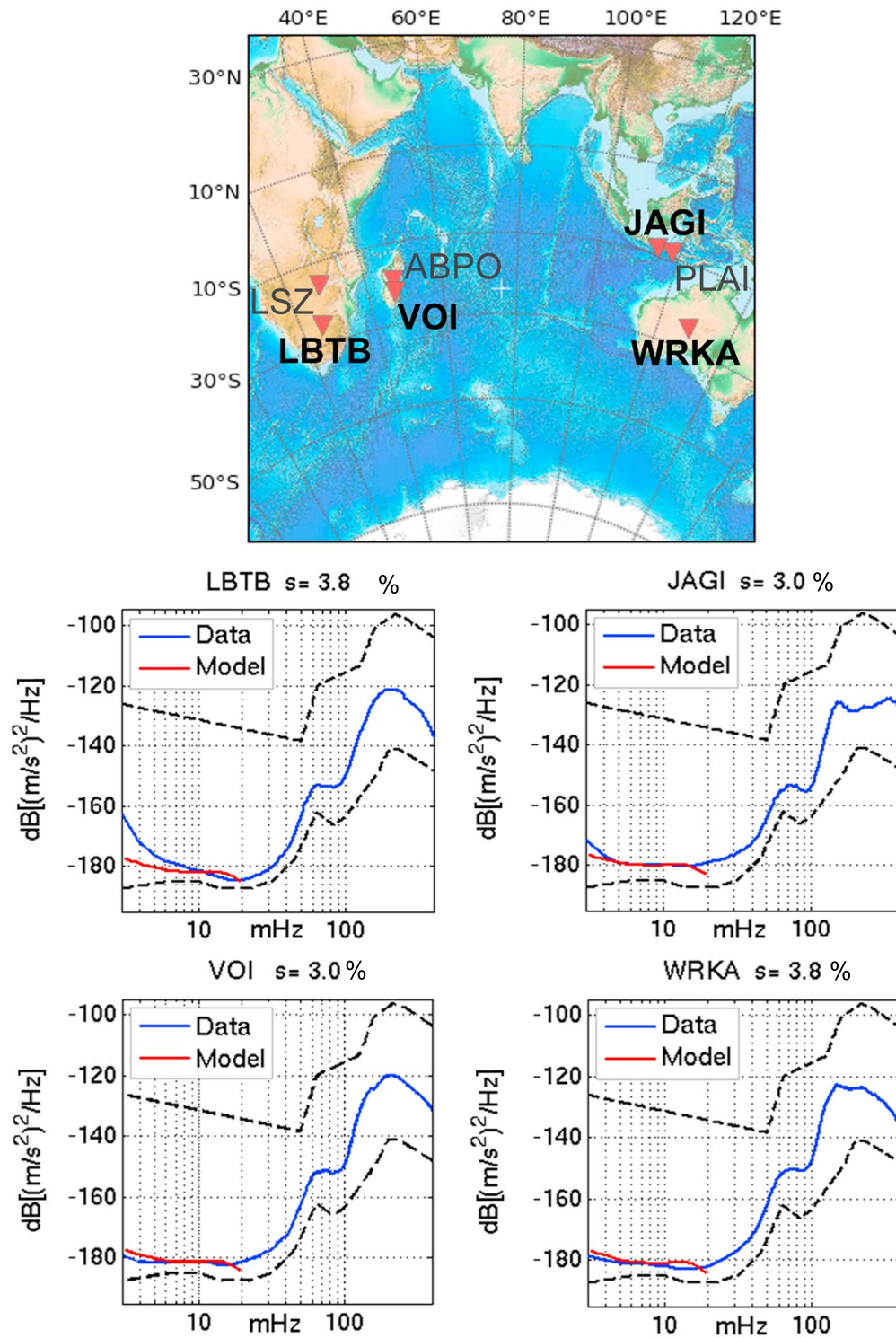


**Figure 2.** Station locations and seismic power spectrum density. Top: Geographical map showing the seismic station locations (downward red triangles) around the Indian Ocean used in this study. Station names are in black. Bottom: Seismic signal power spectrum density in dB with respect to acceleration as a function of frequency for stations ABPO, LBTB, JAGI and WRKA: The annual median of the earthquake free data power spectral density (PSD) is plotted in blue, and the annual median of the synthetic PSD is in red. The maximum frequency of the hum model is 20 mHz (Ardhuin et al., 2015). The high and low noise levels of Peterson (1993) are indicated by dashed lines. The  $s$  values in the title above each seismic PSD are the dimensionless values of equivalent slope factor  $s$  (see equation (3)) used to fit the data amplitude.

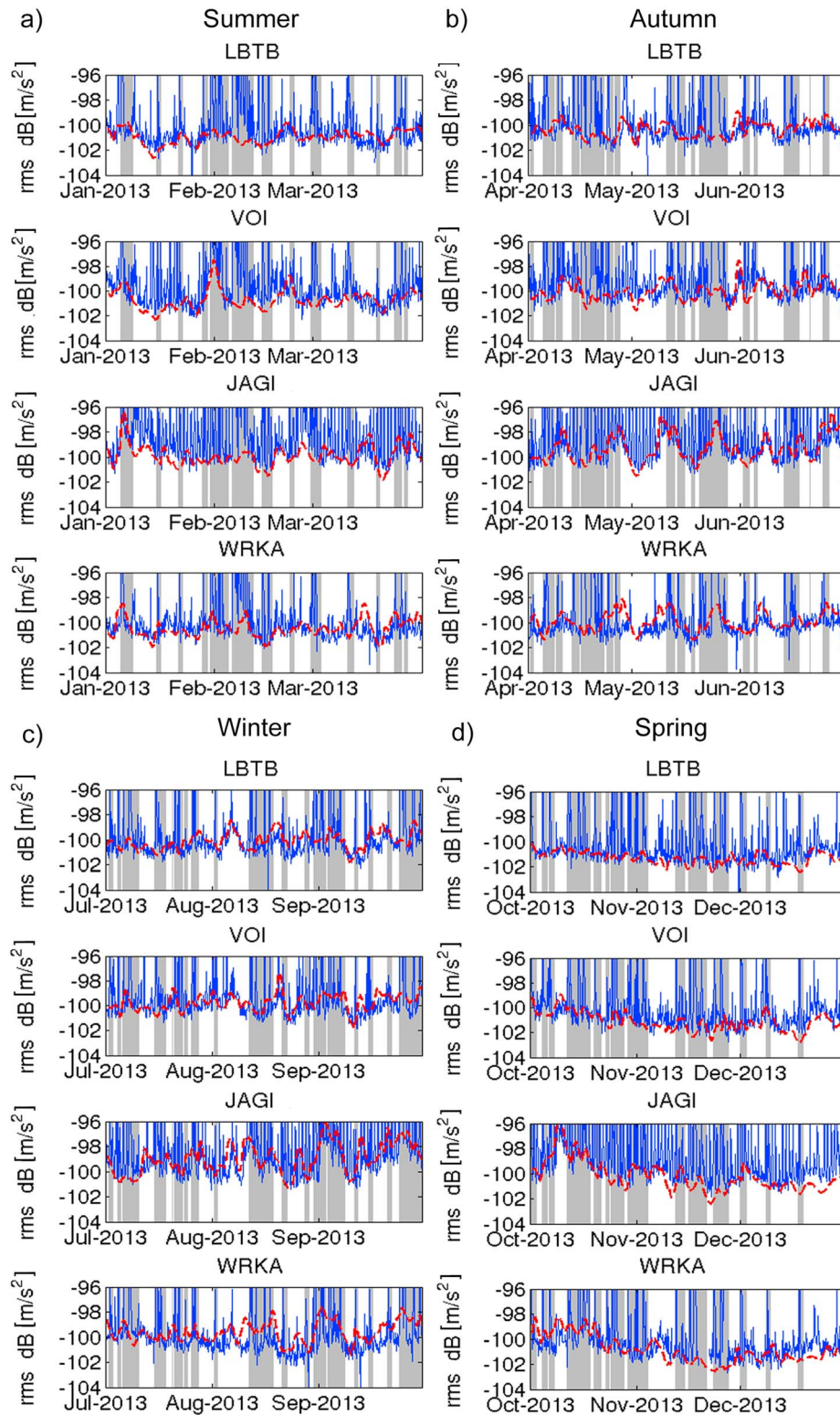


**Figure 3.** Comparison between data and synthetic root-mean-square (RMS) amplitudes for stations mentioned above each plots. In blue is the measured RMS amplitude of the vertical acceleration averaged between 7 and 20 mHz; in red the corresponding synthetic RMS. In gray are times of earthquakes. Plots are split in SH (a) summer, (b) autumn, (c) spring, and (d) winter. All stations show a slight RMS amplitude decrease in the months November and December. We see similar trends for stations on the west of the Indian Ocean (LBTB and VOI) on one side, and for stations on the east (JAGI and WRKA) on the other side. This suggests that the hum is sensitive to local sources in this region.

we consider the baseline of the RMS of the data and the model. The data baseline represents the hum signal that has smooth variations, whereas sudden increases in amplitude of short duration are mostly due to earthquakes.

In Figure 3 we observe a generally good temporal fit between the RMS amplitude of the data and the model. However, at the Australian station WRKA the model seems to occasionally overestimate or underestimate the data. The stations on the west of the Indian Ocean, LBTB and VOI, follow a similar trend over time with the exception of the beginning of February. We will show later (Figure 4) that we can explain this by a local cyclone passing by the station VOI. The stations JAGI and WRKA, located on the east of the Indian Ocean, follow a different pattern from the stations on the west, but similar to each other.

Seasonal variations (in dB with respect to acceleration RMS; Figure 3) are not significant for any of these stations: station LBTB reaches a RMS of just below  $-102$  dB during the SH spring and summer months of November, December, and January; in autumn and winter the RMS gets above  $-99$  dB oscillating around  $-100$  dB. Station VOI (ignoring the signals of cyclones in February and March) oscillates around  $-101$  dB in SH spring and summer and around  $-99$  dB in winter. The RMS of station JAGI goes under  $-100$  dB in SH spring and summer and reaching  $-98$  dB in SH autumn and winter. Station WRKA only leaves its oscillating level of  $-100$  dB to go around  $-101$  dB in November and December. In summary, we observe no significant seasonal variation of the hum recorded in the Indian Ocean.

## 6. Spatial Variations of the Seismic Hum Recorded Around the Indian Ocean

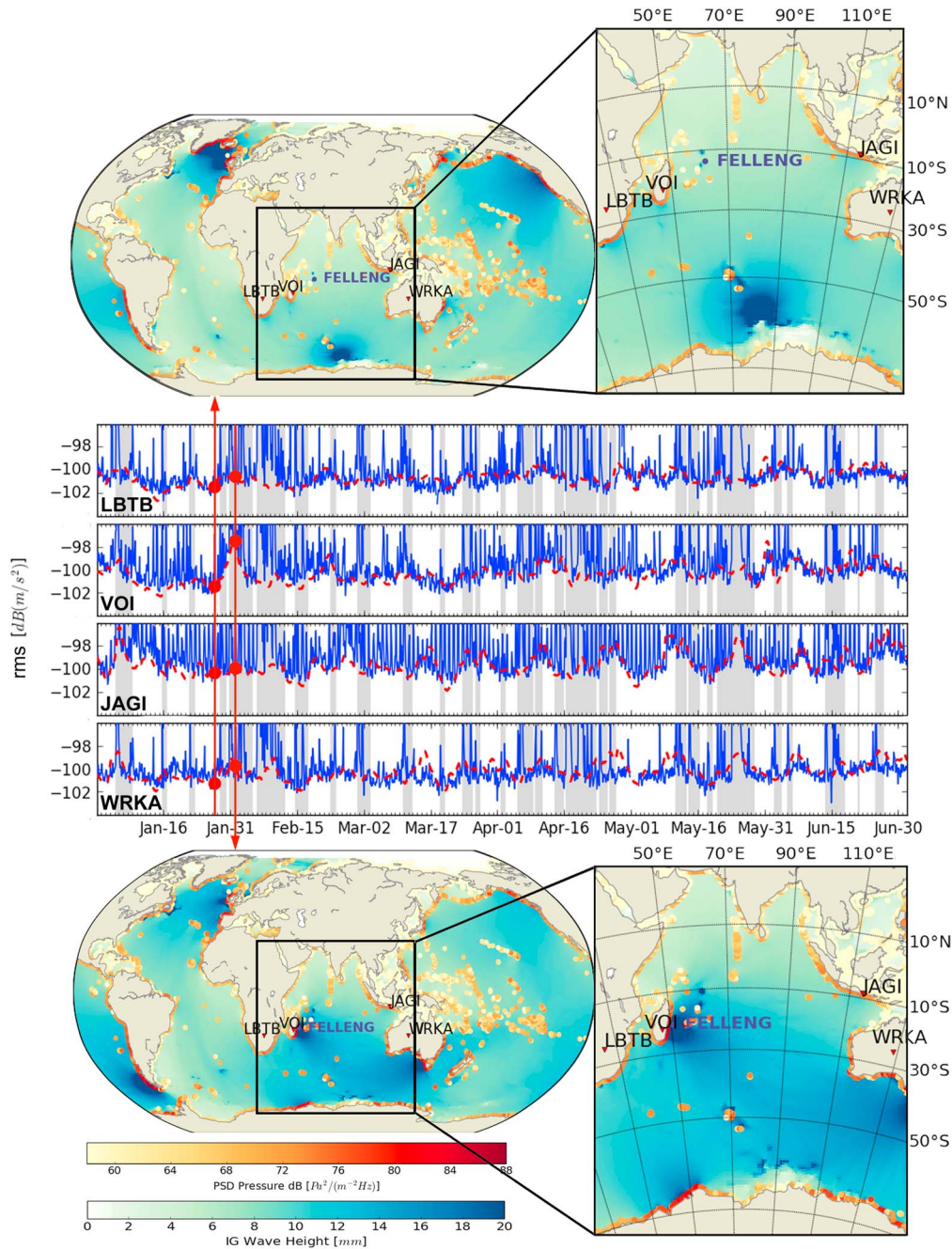
The next step is to localize sources in order to understand the differences in hum amplitudes between the four stations at given times. We do this by investigating during a time lapse the evolution of infragravity wave height and corresponding hum pressure source PSD. We illustrate the influence of a local source on the recorded seismic hum by the example of cyclone Felleng passing the coast of Madagascar in February 2013 (Davy et al., 2016). According to Météo-France Réunion (<http://www.meteofrance.re/cyclone/saisons-passees/>) the cyclone started as a tropical depression on 27 January 2013 and grew to a tropical storm and into a strong tropical cyclone on 30 January 2013. Its intensity started decreasing to a strong tropical storm as it passed close to the coast of Madagascar on 1 February 2013. The entire time lapse sequence and a comparison of the infragravity and the wind sea and swell waveheight for Felleng can be found in the supporting information.

Figure 4 shows two snapshots: before and after the cyclone Felleng reached the coast of Madagascar together with the temporal variation of the seismic hum. We observe that recorded and modeled seismic signal RMS increase between the two times. It is particularly striking for station VOI when the cyclone Felleng propagates toward the station.

On 27 January 2013 at global scale (Figure 4, top plot), we see some particularly strong sources at the east coast of Greenland. In the enlargement of the Indian Ocean, we see no strong source present. On seismic data and model RMS amplitudes, we observe a low RMS level of  $-101$  dB (with respect to acceleration) at all stations. Then, when the cyclone Felleng has arrived at the east coast of Madagascar, it generates relatively high infragravity waves of more than 20 mm (Figure 4, bottom plot). We observe an increase in the hum pressure sources along the same coast, as well as a small increase of pressure sources on the west coast of Australia and Antarctica. At the same time we measure a strong increase of the seismic signal RMS up to  $-98$  at station VOI, compared to only slight increase at the other three stations (up to  $-100$  dB).

Another way to investigate the influence of local sources is by computing the seismic spectra generated by only a given source region. We define four regions (Figure 5): the west of Indian Ocean, the east of Indian Ocean, Antarctica, and the rest of the world. We calculated the seismic signal RMS generated by sources in these regions for two stations on the western (VOI) and eastern (JAGI) side of the Indian Ocean. Seismic spectra RMS averaged between 7 and 20 mHz are plotted in Figure 6.

For the western station VOI, the strongest contribution to the seismic signal in both amplitude and trend is for sources from the western area (cyan). For the eastern station JAGI, sources from the eastern area (dashed green) contribute most to the amplitude and trend of the seismic signal. Further, we see that during SH summer and most of spring, for both stations VOI and JAGI, the contribution of sources outside the Indian Ocean (grey) is stronger than the contribution of sources from the south and from the opposite side of the Indian



**Figure 4.** Influence of a local cyclone generating a strong seismic signal in the hum frequency band at station VOI. Snapshots on 27 January 2013 12:00 and 1 February 2013 00:00 are shown in the top and bottom figures respectively. Infragravity wave heights are plotted with the blue color scale. Circles are the hum pressure sources, and their power spectral densities (PSDs) are plotted with the yellow-red color scale. The location of cyclone Felling is plotted in blue (top plot) and purple (bottom plot). The intensity of the cyclone is moderate when it is blue and strong when it is purple. Seismic root-mean-square (RMS) values are shown in the middle panel for the data (blue) and model (red). The red dots show the signal amplitude, and the red arrows indicate the snapshot at the corresponding time.

Ocean (western sources for JAGI and eastern sources for VOI). During SH winter we see that the second largest contribution of the seismic response is from sources of the opposite side of the Indian Ocean (east for western station VOI and west for eastern station JAGI).

In Figure 7 we compare real and synthetic spectra RMS in a lower frequency band: 3.5–7 mHz.

As previously, the largest contributions to the signal come from the closest sources: western sources for VOI, and eastern sources for JAGI. However, we observe a decrease in the contribution of local sources with

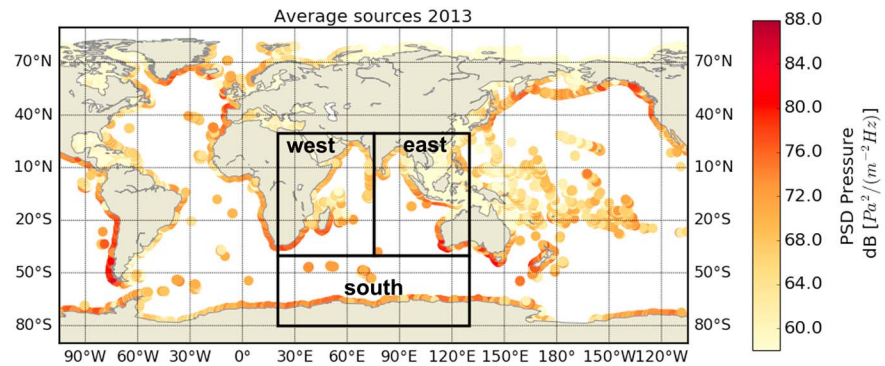


**Figure 5.** Hum source locations used for computing synthetic spectra in Figure 6. Pressure source power spectral density (PSD) averaged in the frequency band 7–20 mHz and over the year 2013 are plotted in color. The west box corresponds to source locations between 30°N–50°S, 20–75°E; the east box considers source locations between 30°N–50°S, 75–130°E; the south box includes sources between 50–80°S, 20–130°E. The rest of the world is the box that contains all source locations outside these three areas.

respect to the total sources in this frequency band, especially during spring and summer. For example, for station VOI the synthetic RMS corresponding to sources outside the Indian Ocean and to western sources occasionally overlap during these two seasons. The general fit between the model and data is less accurate than for frequencies between 7 and 20 mHz (Figure 6) at station JAGI. The model slightly underestimates the recorded signal in summer and spring and slightly overestimates the temporal variations due to local sources. For instance, at the beginning of October, we see an increase in the synthetic hum RMS (red and green curves), but we do not observe the same increase in the data (blue). Station VOI still has a good model-data fit at these low frequencies.

## 7. Discussion

The good fit between the observed and synthetic seismic PSD confirms that pressure sources along the coasts, induced by infragravity waves propagating over a sloping ocean bottom, are the dominant sources of the hum for frequencies between 3.5 and 20 mHz. Infragravity waves are generated by the nonlinear interaction of ocean swells. These swells are generated by winds and therefore follow the general motion of prevailing wind patterns such as westerlies between 30 and 60° south latitudes driving gravity waves to move eastwards. As a result, swells and infragravity waves are strongest on west coasts in the SH, which explains the strong sources there, as seen in Figure 1.

The seismic signal seasonal variations observed in this study are much smaller than what was found by previous global studies (Ekström, 2001; Ermert et al., 2016; Nishida & Fukao, 2007; Rhie & Romanowicz, 2004; Tanimoto & Um, 1999). The lack of a strong seasonal variation in the Indian Ocean is also observed for primary microseisms. Schimmel et al. (2011) and Davy et al. (2015) observed some seasonal variation of the secondary microseisms but no seasonal variations of the primary microseisms recorded in and around the Indian Ocean. The small seasonal variation observed in the hum data is in agreement with the small seasonal variation in the modeled hum sources (pressure PSD) in the Indian Ocean.

We included only the year 2013 in our analysis. Stutzmann et al. (2012) showed that seismic signal, including the hum frequency band, shows no significant variation between years from 2001 to 2011. We further checked that there is no significant change in the hum amplitude after 2013.

Data and model do not always fit perfectly. At the Australian station WRKA the model slightly overestimated the data amplitude. This may be due to different generation mechanisms of infragravity waves over coral reefs (Bertin et al., 2018). Also, we expect that the slope parameter  $s$  in equation (1) should vary spatially. Here instead of using a separate  $s$  for each source location, which would require many more data to be properly constrained, we have adjusted a constant  $s$  separately for each station. This approximation gives an overall good fit of the data, and the values of  $s$  are of the order of what was obtained for real depth profiles (Ardhuin et al., 2015). We expect that the variability of the depth alongshore may further modify the

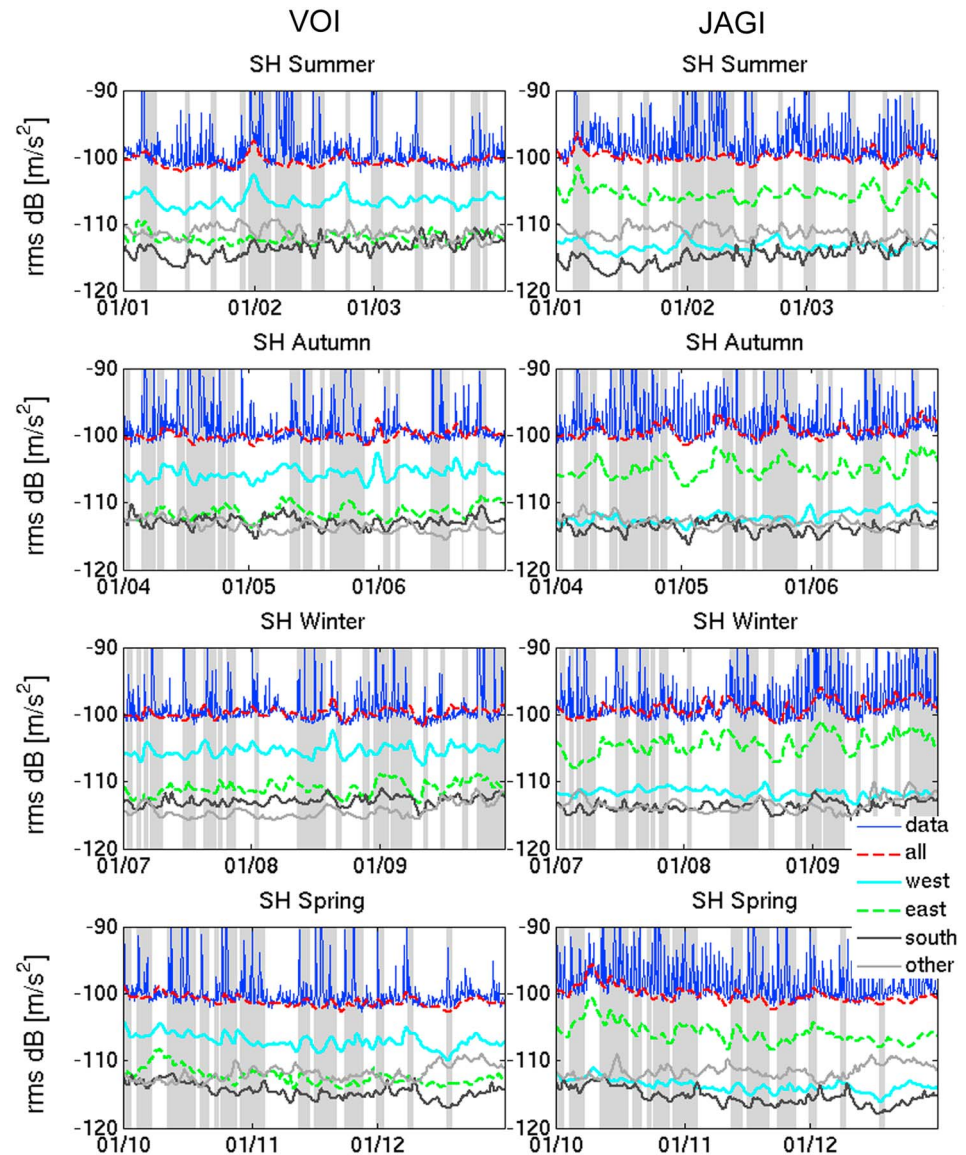


**Figure 6.** Comparison between data and synthetic root-mean-square (RMS) amplitudes averaged between 7 and 20 mHz for sources along the west (cyan) and east (dashed green) coast of the Indian Ocean for the western station VOI (left) and the eastern station JAGI (right). Similar to Figure 3, the RMS amplitude of the vertical acceleration is in blue for the data and in red for the model taking into account all sources of the hum. The RMS acceleration for sources in the south and others are in black and grey, respectively. The source locations west, east, south, and other are shown by squares in Figure 5.

source magnitude and could lead to some interaction with ocean waves that are not perpendicular to the coast. The computation of sources of hum for such cases would require the estimation of the two-dimensional pressure field at the scale of the relevant topography, which is beyond the scope of the present paper (Ardhuin, 2018).

We found a strong contribution of local sources to the recorded seismic signal. When the Tropical Cyclone Felleng passed along the eastern coast of Madagascar, station VOI in Madagascar recorded an elevated hum signal, whereas station LBTB in South Africa continent did not. The most energetic ocean waves did not reach the African main coast due to its protected location behind Madagascar. As a consequence little hum was generated at the African coast, and only a slight increase in hum amplitude was visible at the African station LBTB. This confirms that the hum is only generated when infragravity ocean waves arrive at a coast. Infragravity waves interact with the ocean bottom along Madagascar coasts but can also propagate

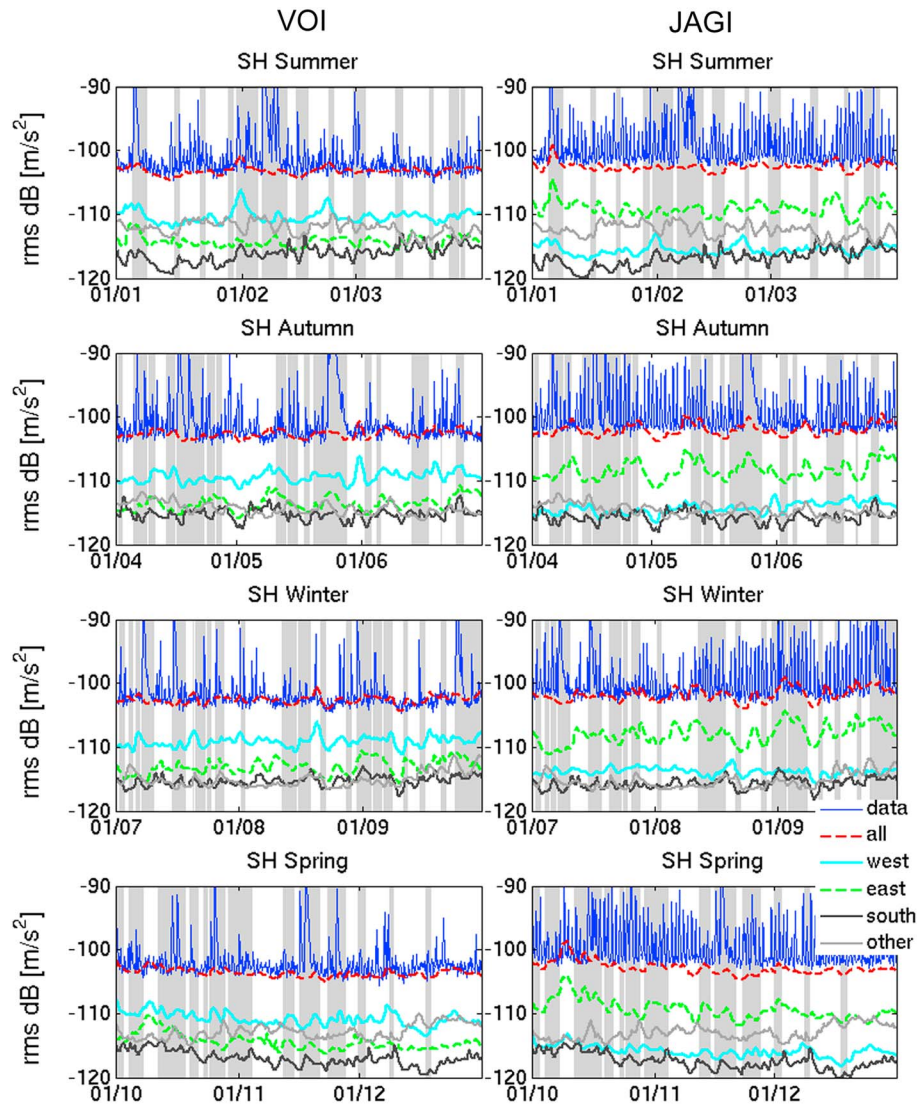


**Figure 7.** Similar to Figure 6 but for frequencies between 3.5 and 7 mHz. The factor  $s$  here is 2.4%, compared to 3 in Figure 6.

across the ocean to the east and generate a hum source at the east of the Indian Ocean. This source is likely much smaller, as we do not observe a large increase in recorded hum signal at stations to the east in the days after the cyclone passed in the west.

### 8. Conclusions

We analyzed the seismic hum recorded around the Indian Ocean in the frequency band 3–20 mHz. We observe no significant seasonal variation of the observed seismic hum PSD. This differs from most studies, performed on a global scale, which reported a global seasonal variation in the hum. We also observed that when cyclone Felleng passed close to the coast of Madagascar, only the nearby station recorded a strong increase of the hum amplitude.

We modeled the seismic hum as Rayleigh waves generated by pressure sources at the ocean bottom along the coasts. These pressure sources are created by the interaction of ocean infragravity waves with the bathymetry slope close to the coast. We use the numerical model of Arduin et al. (2014, 2015) that provides pressure source PSD along coasts in the hum frequency band. We show that the pressure PSD seasonal variations

between 7 and 20 mHz are stronger in the NH, than in the SH. During SH summer, the pressure PSD in the SH is of the same order of magnitude as the pressure PSD in the NH.

We used the pressure PSD source model and computed Rayleigh wave synthetic PSD for seismic stations around the Indian Ocean. We adjusted the fit to the data by empirically determining a slope factor  $s$  that is fixed for each station. We observe a good fit of the temporal variations between data and model in the frequency band 7 and 20 mHz. This good fit confirms that the pressure resulting from the propagation of ocean infragravity waves over the ocean bottom slope at the coast is the mechanism that generates the seismic hum recorded on vertical component.

The synthetic RMS amplitude also reproduces well the strong hum increase on the nearby station when a cyclone is passing along the Madagascar coast. More generally, sources generated along the closest coast to the station provide the strongest signals and there is much less contribution of sources from the other side of the ocean. In the model, we assumed that interaction of seaward moving infragravity waves with the ocean bottom topography accounts for 80% of the sources. The good fit between data and model seems to validate this hypothesis.

To summarize, from our regional study in the Indian Ocean, we show a good fit between measured and modeled seismic hum Rayleigh waves on the vertical component. We observe little seasonal variation and strong influence of sources generated at the nearest coasts. In the future, the modeling should be improved by taking into account more accurately slope factor along each coast. Pressure sources used in this study can explain hum spheroidal modes and Rayleigh waves, but it cannot generate the observed toroidal hum and Love waves for which another mechanism should be quantitatively tested.

#### Acknowledgments

We thank Anya Reading and anonymous reviewers for their reviews that helped us improve the manuscript. We thank the Global Seismic Network (Albuquerque Seismological Laboratory (ASL)/USGS, 1988), the Australian National Seismograph Network (ANSN), the GEOFON seismic network (GEOFON, 1993), and the International Deployment of Accelerometers (IDA) seismic network (Scripps Institute of Oceanography, 1986) for making their data freely available. We extend our thanks to the developers of the freely available software ObsPy (ObsPy version 0.10.2: doi:10.5281/zenodo.17641) and ObspyDMT v2.0.2 (Hosseini, & Sigloch, 2017) that we used to download seismic data. The facilities of IRIS Data Services, and specifically the IRIS Data Management Center, were used for access to waveforms and related metadata used in this study. IRIS Data Services are funded through the Seismological Facilities for the Advancement of Geoscience and EarthScope (SAGE) proposal of the National Science Foundation under Cooperative Agreement EAR-1261681. M. D. would like to thank Martin Gal from the University of Tasmania for sharing insights on the Australian seismic data and data retrieval. This work is funded by ANR MIMOSA (ANR-14-CE01-0012), with additional support from LabexMer via grant ANR-10-LABX-1901. This is IGP contribution number 3981.

#### References

- Albuquerque Seismological Laboratory (ASL)/USGS (1988). Global Seismograph Network (GSN - IRIS/USGS). International Federation of Digital Seismograph Networks. Other/Seismic Network. <https://doi.org/10.7914/SN/IU>
- Ardhuin, F. (2018). Large scale forces under surface gravity waves at a wavy bottom: A mechanism for the generation of primary microseisms. *Geophysical Research Letters*, *45*, 8173–8181. <https://doi.org/10.1029/2018GL078855>
- Ardhuin, F., Gualtieri, L., & Stutzmann, E. (2015). How ocean waves rock the Earth: Two mechanisms explain microseisms with periods 3 to 300 s. *Geophysical Research Letters*, *42*, 765–772. <https://doi.org/10.1002/2014GL062782>
- Ardhuin, F., & Herbers, T. H. C. (2013). Noise generation in the solid Earth, oceans and atmosphere, from nonlinear interacting surface gravity waves in finite depth. *Journal of Fluid Mechanics*, *716*, 316–348. <https://doi.org/10.1017/jfm.2012.548>
- Ardhuin, F., Rawat, A., & Aucan, J. (2014). A numerical model for free infragravity waves: Definition and validation at regional and global scales. *Ocean Modelling*, *77*, 20–32. <https://doi.org/10.1016/j.ocemod.2014.02.006>
- Ardhuin, F., & Roland, A. (2012). Coastal wave reflection, directional spreading, and seismo-acoustic noise sources. *Journal of Geophysical Research*, *117*, C00J20. <https://doi.org/10.1029/2011JC007832>
- Ardhuin, F., Tournadre, J., Queffelec, P., & Girard-Ardhuin, F. (2011). Observation and parameterization of small icebergs: Drifting breakwaters in the southern ocean. *Ocean Modelling*, *39*(3–4), 405–410. <https://doi.org/10.1016/j.ocemod.2011.03.004>
- Aucan, J., & Ardhuin, F. (2013). Infragravity waves in the deep ocean: An upward revision. *Geophysical Research Letters*, *40*, 3435–3439. <https://doi.org/10.1002/grl.50321>
- Barruol, G., & Sigloch, K. (2013). Investigating La Réunion hotspot from crust to core. *Eos, Transactions American Geophysical Union*, *94*(23), 205–207. <https://doi.org/10.1002/2013EO230002>
- Bertin X., de Bakker, A., van Dongeren, A., Coco G., André, G., Ardhuin, F., et al. (2018). Infragravity waves: from driving mechanisms to impacts. *Earth Science Reviews*, (8252). <https://doi.org/10.1016/j.earscirev.2018.01.002>
- Bromirski, P. D., & Gerstoft, P. (2009). Dominant source regions of the Earth's "hum" are coastal. *Geophysical Research Letters*, *36*, L13303. <https://doi.org/10.1029/2009GL038903>
- Davy, C., Barruol, G., Fontaine, F. R., & Cordier, E. (2016). Analyses of extreme swell events on La Réunion Island from microseismic noise. *Geophysical Journal International*, *207*(3), 1767–1782. <https://doi.org/10.1093/gji/ggv365>
- Davy, C., Stutzmann, E., Barruol, G., Fontaine, F. R., & Schimmel, M. (2015). Sources of secondary microseisms in the Indian Ocean. *Geophysical Journal International*, *202*, 1180–1189. <https://doi.org/10.1093/gji/ggv221>
- Deen, M., Wielandt, E., Stutzmann, E., Crawford, W., Barruol, G., & Sigloch, K. (2017). First observations of the Earth's permanent free oscillations on ocean bottom seismometers. *Geophysical Research Letters*, *44*, 10,988–10,996. <https://doi.org/10.1002/2017GL074892>
- Duennebieber, F. K., & Sutton, G. H. (1995). Fidelity of ocean bottom seismic observations. *Marine Geophysical Researches*, *17*(6), 535–555. <https://doi.org/10.1007/BF01204343>
- Durek, J., & Ekstrom, G. (1996). A radial model of anelasticity consistent with long-period surface-wave attenuation. *Bulletin of the Seismological Society of America*, *86*, 144–158.
- Dziewonski, A. M., & Anderson, D. L. (1981). Preliminary reference Earth model. *Physics of the Earth and Planetary Interiors*, *25*(4), 297–356. [https://doi.org/10.1016/0031-9201\(81\)90046-7](https://doi.org/10.1016/0031-9201(81)90046-7)
- Ekström, G. (2001). Time domain analysis of Earth's long-period background seismic radiation. *Journal of Geophysical Research*, *106*, 26,483–26,493. <https://doi.org/10.1029/2000JB000086>
- Ermer, L., Villasenor, A., & Fichtner, A. (2016). Cross-correlation imaging of ambient noise sources. *Geophysical Journal International*, *204*(1), 347–364. <https://doi.org/10.1093/gji/ggv460>
- Fichtner, A. (2014). Source and processing effects on noise correlations. *Geophysical Journal International*, *197*(3), 1527–1531. <https://doi.org/10.1093/gji/ggu093>

- Fukao, Y., Nishida, K., Suda, N., Nawa, K., & Kobayashi, N. (2002). A theory of the Earth's background free oscillations. *Journal of Geophysical Research*, *107*(B9), 2206. <https://doi.org/10.1029/2001JB000153>
- GEOFON Data Centre (1993). GEOFON Seismic Network. Deutsches GeoForschungsZentrum GFZ. Other/Seismic Network. <https://doi.org/10.14470/TR560404>
- Gualtieri, L., Stutzmann, E., Capdeville, Y., Arduin, F., Schimmel, M., Mangeney, A., & Morelli, A. (2013). Modelling secondary microseismic noise by normal mode summation. *Geophysical Journal International*, *193*(3), 1732–1745. <https://doi.org/10.1093/gji/ggt090>
- Haned, A., Stutzmann, E., Schimmel, M., Dizelev, S., Davaille, A., & Yelles-Chaouche, A. (2015). Global tomography using seismic hum. *Geophysical Journal International*, *204*(2), 1222–1236. <https://doi.org/10.1093/gji/ggv516>
- Hasselmann, K. (1962). On the non-linear energy transfer in a gravity-wave spectrum part 1. General theory. *Journal of Fluid Mechanics*, *12*(04), 481–500. <https://doi.org/10.1017/S0022112062000373>
- Hasselmann, K. (1963). A statistical analysis of the generation of microseisms. *Reviews of Geophysics*, *1*, 177–210. <https://doi.org/10.1029/RG001i002p00177>
- Hosseini, K., & Sigloch, K. (2017). ObspyDMT: A Python toolbox for retrieving and processing large seismological data sets. *Solid Earth*, *8*(5), 1047–1070. <https://doi.org/10.5194/se-8-1047-2017>
- Kobayashi, N., & Nishida, K. (1998). Continuous excitation of planetary free oscillations by atmospheric disturbances. *Nature*, *395*(6700), 357–360. <https://doi.org/10.1038/26427>
- Kurrle, D., & Widmer-Schmidrig, R. (2006). Spatiotemporal features of the Earth's background oscillations observed in Central Europe. *Geophysical Research Letters*, *33*, 24304. <https://doi.org/10.1029/2006GL028429>
- Kurrle, D., & Widmer-Schmidrig, R. (2008). The horizontal hum of the Earth: A global background of spheroidal and toroidal modes. *Geophysical Research Letters*, *35*, L06304. <https://doi.org/10.1029/2007GL033125>
- Longuet-Higgins, M., & Stewart, R. (1962). Radiation stress and mass transport in gravity waves, with application to surf beats. *Journal of Fluid Mechanics*, *13*(04), 481–504. <https://doi.org/10.1017/S0022112062000877>
- Longuet-Higgins, M. S. (1950). A theory of the origin of microseisms. *Philosophical Transactions of the Royal Society of London*, *243*(857), 1–35. <https://doi.org/10.1098/rsta.1950.0012>
- Longuet-Higgins, M. S. (1957). On the transformation of a continuous spectrum by refraction. *Proceedings of the Cambridge Philosophical Society*, *53*(01), 226–229. <https://doi.org/10.1017/S0305004100032163>
- Nawa, K., Suda, N., Fukao, Y., Sato, T., Aoyama, Y., & Shibuya, K. (1998). Incessant excitation of the Earth's free oscillations. *Earth, Planets and Space*, *50*(1), 3–8. <https://doi.org/10.1186/BF03352080>
- Neale, J., Harmon, N., & Srokosz, M. (2015). Source regions and reflection of infragravity waves offshore of U.S.'s Pacific Northwest. *Journal of Geophysical Research: Oceans*, *120*, 6474–6491. <https://doi.org/10.1002/2015JC010891>
- Nishida, K. (2013). Earth's background free oscillations. *Annual Review of Earth and Planetary Sciences*, *41*(1), 719–740. <https://doi.org/10.1146/annurev-earth-050212-124020>
- Nishida, K., & Fukao, Y. (2007). Source distribution of Earth's background free oscillations. *Journal of Geophysical Research*, *112*, B06306. <https://doi.org/10.1029/2006JB004720>
- Nishida, K., Kawakatsu, H., Fukao, Y., & Obara, K. (2008). Background Love and Rayleigh waves simultaneously generated at the Pacific Ocean floors. *Geophysical Research Letters*, *35*, L16307. <https://doi.org/10.1029/2008GL034753>
- Nishida, K., & Kobayashi, N. (1999). Statistical features of Earth's continuous free oscillations. *Journal of Geophysical Research*, *104*, 28,741–28,750. <https://doi.org/10.1029/1999JB900286>
- Nishida, K., Montagner, J. P., & Kawakatsu, H. (2009). Global surface wave tomography using seismic hum. *Science*, *326*(5949), 112. <https://doi.org/10.1126/science.1176389>
- O'Reilly, W. C., & Guza, R. T. (1993). A comparison of two spectral wave models in the Southern California Bight. *Coastal Engineering*, *19*(3-4), 263–282. [https://doi.org/10.1016/0378-3839\(93\)90032-4](https://doi.org/10.1016/0378-3839(93)90032-4)
- Peterson, J. (1993). Observation and modeling of seismic background noise. *Geological Survey*.
- Rasche, N., & Arduin, F. (2013). A global wave parameter database for geophysical applications. Part 2: Model validation with improved source term parameterization. *Ocean Modelling*, *70*, 174–188. <https://doi.org/10.1016/j.ocemod.2012.12.001>
- Rawat, A., Arduin, F., Ballu, V., Crawford, W., Corela, C., & Aucan, J. (2014). Infragravity waves across the oceans. *Geophysical Research Letters*, *41*, 7957–7963. <https://doi.org/10.1002/2014GL061604>
- Rhie, J., & Romanowicz, B. (2004). Excitation of Earth's continuous free oscillations by atmosphere–ocean–seafloor coupling. *Nature*, *431*(7008), 552–556. <https://doi.org/10.1038/nature02942>
- Rhie, J., & Romanowicz, B. (2006). A study of the relation between ocean storms and the Earth's hum. *Geochemistry Geophysics, Geophysics*, *7*, Q10004. <https://doi.org/10.1029/2006GC001274>
- Roult, G., & Crawford, W. (2000). Analysis of “background” free oscillations and how to improve resolution by subtracting the atmospheric pressure signal. *Physics of the Earth and Planetary Interiors*, *121*(3-4), 325–338. [https://doi.org/10.1016/S0031-9201\(00\)00172-2](https://doi.org/10.1016/S0031-9201(00)00172-2)
- Saha, S., Moorthi, S., Pan, H. L., Wu, X., Wang, J., Nadiga, S., et al. (2010). The NCEP Climate Forecast System Reanalysis. *Bulletin of the American Meteorological Society*, *91*(8), 1015–1058. <https://doi.org/10.1175/2010BAMS3001.1>
- Schimmel, M., Stutzmann, E., Arduin, F., & Gallart, J. (2011). Earth's ambient microseismic noise. *Geochemistry, Geophysics, Geosystems*, *12*, Q07014. <https://doi.org/10.1029/2011GC003661>
- Scripps Institution of Oceanography (1986). IRIS/IDA seismic network. International Federation of Digital Seismograph Networks. Other/seismic network. <https://doi.org/10.7914/SN/II>
- Stutzmann, E., Arduin, F., Schimmel, M., Mangeney, A., & Patau, G. (2012). Modelling long-term seismic noise in various environment. *Geophysical Journal International*, *191*(2), 707–722. <https://doi.org/10.1111/j.1365-246X.2012.05638.x>
- Stutzmann, E., Roult, G., & Astiz, L. (2000). Geoscope station noise level. *Bulletin of the Seismological Society of America*, *90*(3), 690–701. <https://doi.org/10.1785/0119990025>
- Suda, N., Nawa, K., & Fukao, Y. (1998). Earth's background free oscillations. *Science*, *279*(5359), 2089–2091. <https://doi.org/10.1126/science.279.5359.2089>
- Tanimoto, T. (2005). The oceanic excitation hypothesis for the continuous oscillations of the Earth. *Geophysical Journal International*, *160*, 276–288.
- Tanimoto, T., & Um, J. (1999). Cause of continuous oscillations of the Earth. *Journal of Geophysical Research*, *104*, 28,723–28,739. <https://doi.org/10.1029/1999JB900252>
- Tanimoto, T., Um, J., Nishida, K., & Kobayashi, N. (1998). Earth's continuous oscillations observed on seismically quiet days. *Geophysical Research Letters*, *25*, 1553–1556. <https://doi.org/10.1029/98GL01223>

- Tolman, H., Accensi, M., Alves, H., Arduin, F., Bidlot, J., Boojij, N., et al. (2014). User manual and system documentation of WAVEWATCH III™ version 4.18., NOAA/NWS/NCEP/MMAB Tech. Rep., 194(316).
- Tournadre, J., Bouhier, N., Girard-Arduin, F., & Rémy, F. (2016). Antarctic icebergs distributions 1992–2014. *Journal of Geophysical Research: Oceans*, 121, 327–349. <https://doi.org/10.1002/2015JC011178>
- Traer, J., & Gerstoft, P. (2014). A unified theory of microseisms and hum. *Journal of Geophysical Research: Solid Earth*, 119, 3317–3339. <https://doi.org/10.1002/2013JB010504>
- Tromp, J., Luo, Y., Hanasoge, S., & Peter, D. (2010). Noise cross-correlation sensitivity kernels. *Geophysical Journal International*, 183(2), 791–819. <https://doi.org/10.1111/j.1365-246X.2010.04721.x>
- Webb, S. C. (2007). The Earth's "hum" is driven by ocean waves over the continental shelves. *Nature*, 445(7129), 754–756. <https://doi.org/10.1038/nature05536>
- Webb, S. C. (2008). The Earth's hum: The excitation of Earth normal modes by ocean waves. *Geophysical Journal International*, 174(2), 542–566. <https://doi.org/10.1111/j.1362-246X.2008.03801.x>
- Widmer-Schmidrig, R. (2003). What can superconducting gravimeters contribute to normal-mode seismology? *Bulletin of the Seismological Society of America*, 93(3), 1370–1380. <https://doi.org/10.1785/0120020149>